

This document is the accepted manuscript version of the following article:

Giannakopoulos, G. K., Keskinen, K., Koch, J., Frouzakis, C. E., Wright, Y. M., & Boulouchos, K. (2022). Characterizing the evolution of boundary layers in IC engines by combined direct numerical and large-eddy simulations. *Flow, Turbulence and Combustion*. <https://doi.org/10.1007/s10494-022-00383-1>

Characterizing the evolution of boundary layers in IC engines by combined direct numerical and large-eddy simulations

George K. Giannakopoulos^{1,2*}, Karri Keskinen^{1,3}, Jann Koch¹, Christos E. Frouzakis^{1,2}, Yuri M. Wright^{1,4} and Konstantinos Boulouchos¹

¹Aerothermochemistry and Combustion Systems Laboratory, ETH Zurich, Switzerland.

²Combustion and Acoustics for Power & Propulsion Systems, ETH Zurich, Switzerland.

³Department of Mechanical Engineering, Aalto University, Finland.

⁴Empa, Swiss Federal Laboratories for Materials Science and Technology, Automotive Powertrain Technologies, Switzerland.

*Corresponding author(s). E-mail(s): georgeg@ethz.ch;
Contributing authors: karri.keskinen@aalto.fi; cfrouzakis@ethz.ch;
ywright@ethz.ch; kboulouchos@ethz.ch;

Abstract

The structure of boundary layers (BLs) and wall heat flux is investigated as they evolve during the compression stroke in an optically accessible, single-cylinder research engine of passenger-car dimensions with a typical four-valve pent-roof design operated at motored and throttled conditions. Three-dimensional Direct Numerical Simulations (DNS) of the compression stroke were carried out, which enable full resolution in space and time of all flow and temperature field structures in the entire domain, including the BLs. Since the high computational cost precludes calculation of the scavenging cycle, scale-resolving simulations were employed to provide initial fields for the DNS at intake valve closure. The analysis revealed that BLs deviate from ideal scaling laws commonly adopted in algebraic wall models, and that the non-zero streamwise pressure gradient correlates with changes in the near-wall profiles. Phenomenologically,

such deviations are similar to those for developing BLs, and in particular for impinging flows. The momentum BL structure was found to be affected by the large-scale bulk flow motion, in contrast to the thermal BLs which exhibit a more structured behavior following the density increase due to compression. Inspection of the heat flux distribution confirmed the similarity between the flow and heat flux patterns and identified regions of intense heat flux, mainly in locations of strong directed flow towards the wall. The improved characterization of the boundary layer structure and its evolution during the compression stroke not only constitutes an important step towards improved understanding of near-wall phenomena in internal combustion engines, but the vast dataset also serves as a database for development of improved wall models.

Keywords: direct numerical simulation, internal combustion engine, boundary layer, wall heat transfer, near-wall scaling

1 Introduction

The gas motion inside the combustion chamber of internal combustion engines (ICEs) has a profound influence on the overall engine efficiency and performance. The formation of both large- and small-scale flow patterns is the result of a series of complex interacting phenomena taking place during engine operation (intake valve jets, compression/expansion, interaction with the chamber walls etc.), rendering its understanding one of the most challenging tasks in technical applications today [1–4].

Not surprisingly, the importance of near-wall phenomena in ICEs was recognized early on and has attracted considerable interest over the years, mainly due to their direct relation with the engine heat losses [5]. Characterization of near-wall processes within the BL has become possible with significantly improved spatial and temporal resolution by recent advances in optical diagnostics techniques. Detailed insights into the BL structure and its coupling with the in-cylinder flow can be found in [6–9] where a combination of high speed particle image velocimetry (PIV) and particle tracking velocimetry (PTV) was used. These techniques allow for the characterization of the two-dimensional velocity field and the identification of small vortical structures within the boundary layer that promote fluid exchange with the bulk flow.

In parallel, the establishment of scale-resolving methodologies for the study of ICE flows enabled the fundamental exploration of in-cylinder physical processes [10], but at the same time revealed the need for detailed validation data for further model development and testing. To address this need, experimental groups focused on building “modeling-friendly” experimental setups, featuring well-characterized geometries and boundary conditions. The two most prominent ones are the Transparent Combustion Chamber (TCC) engine of the University of Michigan, [11] and the TUDa engine at TU Darmstadt [12]. The main difference between the two lies on the cylinder head geometry: a

flat, pancake-shaped design promoting a swirling in-cylinder flow and a more complex, pent-roof geometry inducing a strong tumble flow, respectively.

With the abundance of high-quality validation data, substantial numerical work has been conducted on the wall-guided cylinder head variant of the TUDa engine at motored operation: Baumann et al. [13] compared predictions from 50 LES cycles with Particle Image Velocimetry (PIV) data for two grid resolutions, showing good agreement for the phase-averaged and RMS velocities. Di Mare et al. [14] used the same setup to characterize the adequacy of various LES quality metrics, while Nguyen et al. [15] used two numerical codes to investigate the influence of grid structure and numerical schemes, observing comparable results for both approaches. Janas et al. [16] compared LES predictions to both PIV data from the engine as well as to Magnetic Resonance Velocimetry data in the valve seat region of a static dummy setup to study the inflow conditions. Additionally, a method to quantify the tumble breakdown process was proposed using a small number of cycles. He et al. [17] examined the anisotropy of the in-cylinder turbulence, observing a high degree during the intake stroke, whereas the compression stroke was found to be more isotropic up to the initiation of the tumble breakdown that introduced additional anisotropic structures. Buhl et al. [18] compared different approaches of modeling the intake and exhaust ports. For the three variants tested, no significant influence on the accuracy of the predicted flow fields was found at the considered turning speed of 800 rpm. Janas et al. [19] also performed LES of a reactive operating point in order to study the penetration of the flame into the top-land crevice, highlighting the necessity of including the crevice volume in numerical simulations for Bowditch-type optically accessible engines.

Wall modeling has become a focal point in contemporary LES and highlighted as a key technological aspect towards simulating realistic engineering applications (e.g. [20, 21]). Much of the recent work focuses on high Reynolds number academic configurations or aerodynamically motivated test cases, while ICE applications are comparatively less studied. The challenging near-wall region is often treated using wall functions. Even in academic wall-modeled LES (WMLES), best practices are still being established as modeling errors result from different hypotheses and require different remedies [22]. Furthermore, compared to wall stress modeling, wall heat transfer models are much less developed [20]. This relates especially to complex flow locations where the Reynolds analogy (typically assumed in algebraic wall functions) is not applicable, i.e. where wall heat flux and wall shear stress are not correlated, as was shown in a recent LES study of pulsed hot jets impinging on a cold wall [23].

Beyond well-known global correlations (e.g. [24–26]) and algebraic models (e.g. [27–30]), a modern approach in LES is based on simplified forms of the momentum and thermal turbulent boundary layer equations (TBLEs) within the inner part of the BL [21]. Approaches are either based on equilibrium assumptions (akin to many algebraic wall functions), or attempt to account for non-equilibrium effects (e.g. [31, 32]). Recent developments also

include novel approaches such as boundary layer parametrization [33, 34] and slip-wall boundary conditions [35]. While near-wall scaling improvements have been achieved in compressible configurations with near-wall material property variations [36, 37], the unique phenomenology surrounding ICE boundary layers results in a much more challenging setup. Specifically, near-wall structures are conspicuously governed by impingement and ejection processes, resulting in considerable departure from conventional developed boundary layers (e.g., [38]).

Recent advances in scalable computational methods and tools, as well as the availability of high-performance computing, have enabled application of direct numerical simulations (DNS) to engine-relevant geometries [39]. However, the need for sophisticated tools that combine highly accurate spatio-temporal discretization schemes with the geometric flexibility to capture the ICE geometry, has made such studies rare. More importantly, the associated computational cost has limited those studies to simplified geometries and to conditions which are far from those encountered during normal engine operation. In spite of these limitations, fundamental knowledge has been acquired and unique datasets for model development and validation have been generated. Specifically with respect to boundary layers in ICEs, [38, 40–43] report on the structure of the near-wall velocity and temperature profiles and the impact of wall heat transfer on the evolution of temperature stratification in the bulk.

Current views and points of further development are illustrated by two recent wall-modeling studies, employing reference data from experiments [44] and DNS [45]. Both studies strongly indicate the inapplicability of standard wall laws for ICEs. The first study implies that incorporating non-equilibrium effects like the wall-parallel pressure gradient results in improved wall friction and heat transfer predictions. In the scale-resolving numerical study [45], the DNS near-wall scaling was recovered quite well when a zonal LES/RANS hybrid was combined with a non-equilibrium TBLE model. The model attempts to probe the near-wall vicinity and shape near-wall profiles based on the indicated surrounding flow type.

While such results are promising, the type of non-equilibrium model optimal to ICE remains an open question. Moreover, both studies face limitations: the experimental data used in [44] are limited in terms of spatial extent and only ensemble-averaged inputs were employed. The numerical study [45] provides a more complete overview of its physical domain, but the setup is a strongly simplified engine configuration. In addition, the Reynolds numbers in both studies are below the expected range of either high speed (automotive) or large (marine) engines. A wealth of a priori information is available purely from the analysis of high-fidelity experimental or numerical datasets. However, for use in engine CFD, a posteriori work is additionally mandated by the documented dependence between numerics and wall-modeling approaches [20]. In other words, data-driven hypotheses and models derived therein need to be tested in actual wall-modeled LES configurations. As it stands, the lack

of scale-resolving, modeling-focussed studies in the most engineering-relevant conditions forms a clear research gap.

1.1 Study objectives and adopted workflow

The engine configuration used in this work is the optically-accessible, single-cylinder engine of TU Darmstadt, which has been designed to provide well-defined boundary conditions and reproducible operation [12]. The engine is equipped with a four-valve cylinder head and an inlet duct designed to create a tumble flow. The present study focuses on motored operation at an engine speed of 800 rpm and intake pressure of 0.4 bar. The bulk Reynolds number based on the bore, the mean piston speed and air viscosity evaluated at the wall temperature, indicative of the large scale flow, is $Re = BV_{p,mean}/\nu_{air} = 16,847$. For the experimental characterization of the in-cylinder flow, a combined PIV/PTV setup was used to simultaneously capture the crank angle resolved flow above the piston at high resolution, as well as that of the global flow [6, 12].

The main objective of this work is to investigate the structure of the momentum and thermal boundary layers as they evolve during the compression stroke in the spray guided variant of the TUDa engine using DNS. Due to computational cost limitations, the simulation of the gas exchange process at realistic conditions is still beyond reach for DNS. In order to generate representative initial conditions, a workflow exploiting the complementarity between experiments and different simulation methodologies has been adopted as shown schematically in Fig. 1.

Multiple consecutive cycles were simulated using scale-resolving methodologies to acquire a sufficient statistical sample that allows comparison with the available experimental data. The extracted phase-averaged flow field was compared against the corresponding multi-cycle PIV measurements to ensure that the model captures adequately the major flow features throughout the cycle. The intake stroke of a single cycle was then simulated on a refined grid in order to generate an initial condition for the DNS at intake valve closure (IVC) with low modeled contribution. This is an essential step in the process, since the simulation of multiple cycles of the full gas exchange (i.e. including the intake and exhaust strokes) for such a complex geometry and conditions using DNS carries a currently impractically high computational cost. Indicatively, previous multi-cycle simulation campaigns on the TCC engine [46] employing similar numerical methodology (albeit not DNS) exhibited a highly uneven computational cost distribution throughout the cycle, with the gas exchange process accounting for 85% of the total simulation time, attributed mainly to stringent resolution (and correspondingly time step) requirements to adequately resolve the high velocity valve jet flow.

Following the successful initialization at IVC, the evolution of all relevant time and length scales during the compression stroke are simulated with DNS in Sec. 3, providing much needed data for the physical understanding of the

complex interaction of the flow and temperature in the bulk as well as in the wall vicinity.

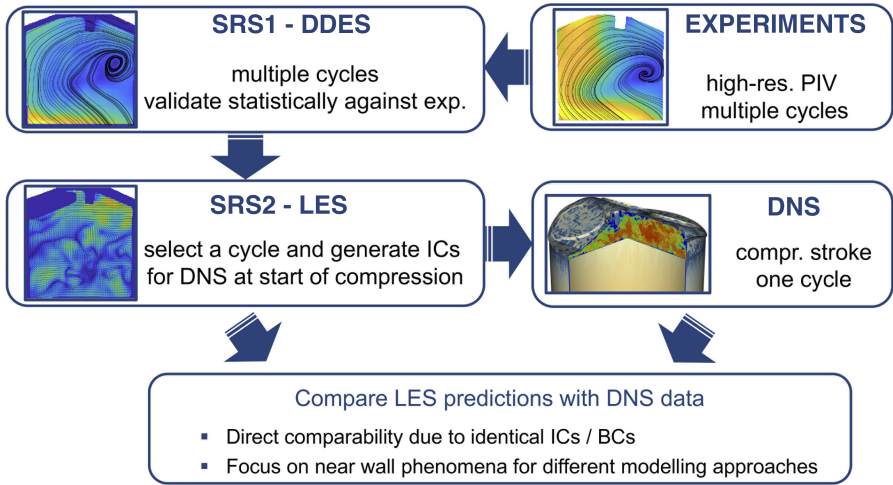


Fig. 1: Schematic representation of the adopted workflow to generate initial conditions for the DNS of the compression stroke.

2 Multi-cycle scale-resolving simulations

Scale-resolving simulations (SRS) preceding the DNS were carried out for the TUDa engine geometry in two configurations: SRS1 is a multi-cycle simulation with a relatively coarse grid, while SRS2 denotes an intake stroke simulation with a finer grid. A total of 28 consecutive cycles were computed in SRS1, of which the first three were discarded to remove the initial condition influence, similar to [47]. From the remaining 25 cycles, the field of the third cycle at TDC (360 crank angle degrees (CAD), i.e. at end of the exhaust stroke) was mapped onto the fine grid and used as a starting point for SRS2, whose purpose is to generate the initial condition for the DNS at inlet valve closure (IVC at 590 CAD) with a low modeled contribution. The methodology for SRS1 and SRS2 is briefly presented in Sec. 2.1, followed by a comparison between SRS1 and PIV measurements in Sec. 2.2.

2.1 Numerical methodology

The STAR-CD v4.30 finite volume solver is used in conjunction with the es-ICE plug-in to account for the mesh motion. The large intake and exhaust runners are meshed at a resolution of 2 mm. Mesh resolution is gradually refined towards the valves, while the in-cylinder cell size is set to 1 mm for SRS1 (similar to [47] and [14]), and 0.5 mm for SRS2, leading to an overall cell

count at BDC of 1.4×10^6 and 7.0×10^6 , respectively. For both cases, a prism layer of thickness 0.2 mm at the walls results in $y^+ = O(1)$ through most of the cycle, with values of $y^+ = O(10)$ expected during late compression.

The monotone advection reconstruction scheme (MARS) is used for spatial discretization with compression levels of 0.5 (SRS1) and 0.75 (SRS2), where a higher value denotes better ability to capture sharp discontinuities. In both cases, STAR-CD employs a temporal scheme based on the fully-implicit Euler scheme and explicit deferred correctors. The pressure-implicit splitting of operators (PISO) method is used for the pressure-velocity coupling. We note that in scale-resolving CFD simulations, it would be ideal to employ high-order numerical schemes. While some successful efforts in specific numerical frameworks have been presented in the literature (e.g. [48]), higher order numerics are scarce in scale-resolving ICE simulations due to grid complexity [49]. Time-varying pressure and temperature conditions are applied at the intake and exhaust boundary, derived from a GT-power model that was validated by means of phase-averaged pressure measurements [50]. The maintenance temperature of $T_w = 333$ K is applied as a Dirichlet condition on all wall boundaries.

In SRS1, a delayed detached eddy simulation (DDES) methodology based on the low-Reynolds $k - \omega$ SST model is adopted in its standard form. A similar approach was successfully employed by Hasse et al. [51] in a simplified engine setup. As the near-wall grid resolution is not always within the low-Reynolds region of applicability, the wall boundaries are treated with a hybrid wall model

$$\tau_w = (1 - \xi) \tau_w^{LR} + \xi \tau_w^{HR} \quad (1)$$

where superscripts LR and HR refer to low-Reynolds and high-Reynolds definitions, respectively, and the blending factor ξ is determined via a first estimate of y^+ using Spalding's law [52]. A similar blending procedure is incorporated for the wall heat flux model. The higher-resolution SRS2 employs wall-modeled LES (WMLES) using a transported k_{sgs} model for the unresolved scales. The built-in wall stress and heat transfer models by Plensgaard and Rutland [53] in Star-CD are used in their original formulations with modeling constants $c_{mw} = 0.01$ and $c_{hw} = 0.8$. It should be pointed out that the SRS1 and SRS2 computations employ fairly basic wall models and there is a need for improved models in engine configurations. However, models involving, for example, non-equilibrium effects are far from mainstream in contemporary scale-resolving simulations of engine flows.

The simulations were performed with time steps of 0.025-0.05 CAD (SRS1) and 0.01-0.02 CAD (SRS2). The computational cost for a single cycle of SRS1 was about 1,070 CPU core-hours (ca. 15 wall-clock hours on 72 cores), while SRS2 expended about 12,000 CPU core-hours between 380 and 590 CAD.

2.2 Flow field comparison between SRS1 and PIV measurements

The multi-cycle SRS1 simulation is compared with the ensemble-averaged PIV measurements to ascertain that the main flow features in the process are suitably represented by the computation. For this purpose, the flow fields are quantitatively compared. Instead of observing flow profiles at specific lines (akin to [47]), the entire PIV field of view (FOV) is used for comparison. PIV flow field data has been measured at two planes, the spark plane ($y = 0$) and the valve plane ($y = -19$ mm).¹

The phase-averaged simulated flow field from SRS1 is interpolated onto the PIV grid, yielding vector fields that can be directly compared. The vector field correspondence is quantified using the relevance index (RI) [54] and magnitude index (MI) [55]

$$RI = \frac{\langle u_{SRS1} \rangle \cdot \langle u_{PIV} \rangle}{\|u_{SRS1}\| \cdot \|u_{PIV}\|} \quad (2)$$

$$MI = 1 - \frac{\|\langle u_{SRS1} \rangle - \langle u_{PIV} \rangle\|}{\|\langle u_{SRS1} \rangle\| + \|\langle u_{PIV} \rangle\|} \quad (3)$$

where angled brackets denote phase-averaging and velocity field components on the $x - z$ -plane are considered. $RI \in [-1, 1]$ denotes the orientation correspondence between vector fields, while $MI \in [0, 1]$ is determined through both orientation and magnitude correspondence. Hence, $RI = 1$ represents perfect correspondence in orientation, while $MI = 1$ denotes perfect correspondence in both orientation and magnitude. In practice, MI is a more stringent metric, as noted in [56].

Figures 2 and 3 display the phase-averaged planar velocity fields from SRS1 and PIV, along with local RI and MI values at mid-compression (630 CAD). During compression, the dominant tumble vortex is well represented by SRS1 on both observation planes. As can be noted in the RI plot, the flow orientation correspondence is particularly strong. Furthermore, the local metrics highlight the slight inaccuracy in the vortex centre positioning, represented by the region of low RI and MI values.

Flow field correspondence varies with time, as displayed in Fig. 4 at 480 CAD exhibiting similarity of the large-scale flow features with different strengths of the intake jets. The correspondence is exemplified in Figs. 2-4 for the entire gas exchange process, while Fig. 5 depicts the average RI and MI values on the spark and valve planes. Correspondence between SRS1 and PIV is generally highest during mid-intake and mid-compression. It should be noted however, that as the PIV field of view changes with piston position, a smaller fraction of the flow field is analyzed close to TDC.

To summarise, the SRS1 and PIV velocity fields have very good orientation correspondence, while in terms of magnitudes the match is slightly inferior. The results suggest that the main flow features are adequately captured by

¹The z -axis is in the cylinder center and points to the piston, while the x -axis is directed from the intake to the exhaust side; the valve plane cuts through both intake and exhaust valves.

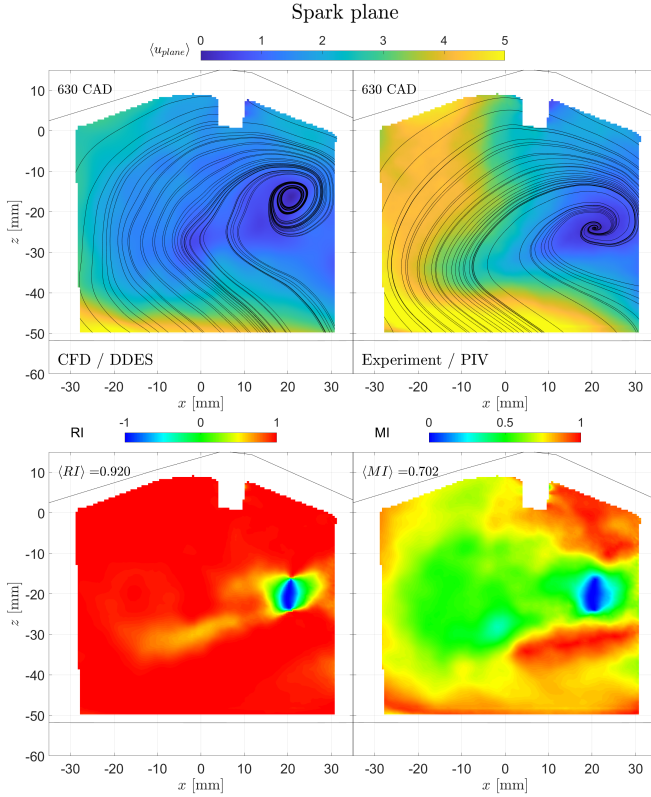


Fig. 2: Top: comparison between phase-averaged mean flow fields in the SRS1 computation (25 cycles) and PIV measurement (74 cycles) in the spark plane, midway through the compression stroke at 630 CAD. Bottom: local values of the relevance index (RI) and the magnitude index (MI) for the velocity fields; their mean values are denoted by angled brackets.

the LES, as expected from previous studies with similar grid resolutions [47], forming a good baseline for SRS2 and the subsequent DNS.

3 DNS of the compression stroke

3.1 Numerical methodology

In the DNS, the governing equations are discretized in space using the spectral element method [57] in a computational domain that is split globally into unstructured conforming hexahedral elements, while locally the geometry and solution are expressed as 7th-order tensor product Lagrange polynomials evaluated at the Gauss-Lobatto-Legendre (GLL) quadrature points [57]. Combining the high-order accuracy of spectral methods with the geometric flexibility of finite elements, the method is perfectly suited for high-fidelity

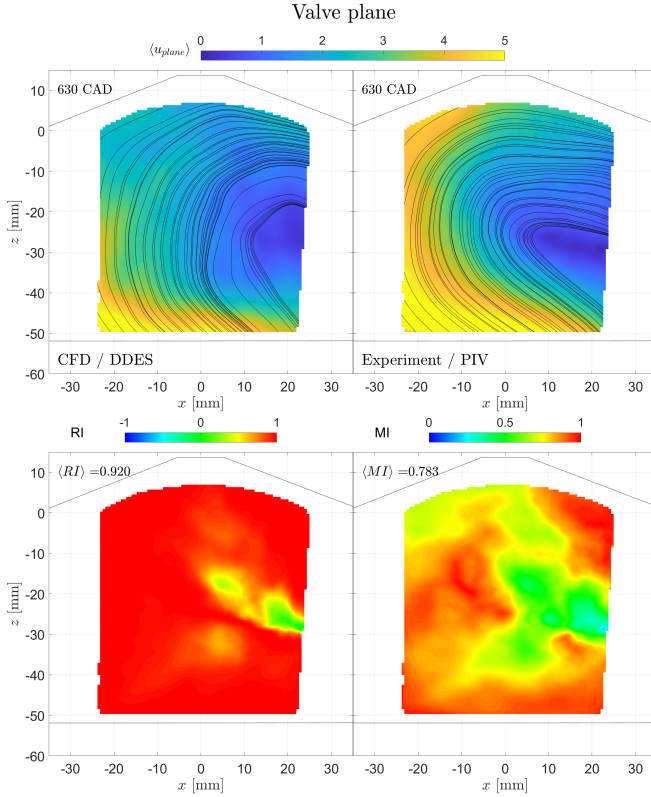


Fig. 3: Top: comparison between phase-averaged mean flow fields in the SRS1 computation (25 cycles) and PIV measurement (74 cycles) on the valve plane, midway through the compression stroke at 630 CAD. Bottom: local values of the relevance index (RI) and the magnitude index (MI) for the velocity fields; their mean values are denoted by angled brackets.

simulations in complex geometries. The discretized equations are integrated in time using Nek5000 [58], a highly-efficient and massively parallel low-Mach number flow solver, which has been used to perform DNS and WRLES studies of engine-relevant phenomena [38, 40–43, 46, 59, 60].

In contrast to Star-CD, Nek5000 requires a conformal hexahedral grid, a precondition that renders this task highly non trivial. In-house algorithms were developed and used in combination with Trelis [61] for the generation of computational grids that accurately capture the complex geometric features of the engine, while satisfying the necessary mesh quality criteria. The grids were constructed by meshing the cylinder head volume with tetrahedral elements, which were subsequently split into conforming hexahedra. Next, for the grid generation for the cylinder and crevice volumes, the mesh at the lower surface of the head was extruded axially to form tensor-product element layers that can accommodate the vertical mesh deformation due to the piston motion without

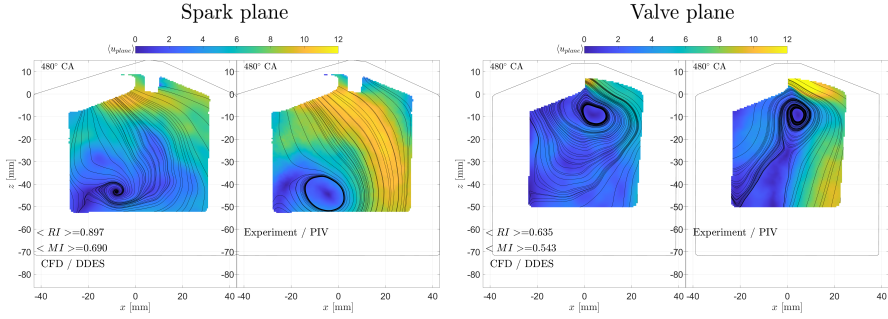


Fig. 4: Comparison between phase-averaged mean flow fields in the SRS1 computation (25 cycles) and PIV measurement (74 cycles) on the spark (left) and valve plane (right) during the intake stroke at 480 CAD.

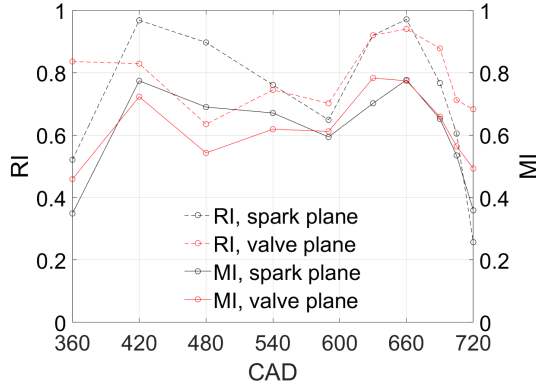


Fig. 5: Evolution of the average RI and MI values between SRS1 and the experiment throughout the intake (360 to 540 CAD) and compression (540 to 720 CAD) strokes.

high distortion. In order to ensure that the momentum and thermal boundary layers are fully resolved, additional refinement layers were added close to the walls. Finally, a Laplacian smoother was applied to improve mesh quality.

Following this approach, in order to ensure adequate resolution throughout the cycle, where the flow Reynolds number increases and the turbulent scales become smaller during compression, two grids with 1.6 million and 2.1 million spectral elements were constructed, resulting in 560 million and 714 million unique grid points, respectively, for the employed 7th-order polynomials. An average mesh resolution of 40 μm was attained in the bulk, with the first grid point located at most 5 μm away from the walls. A posteriori computation of the wall shear stress confirmed that y^+ values much lower than 1 were attained at all times.

The Arbitrary Lagrangian Eulerian (ALE) formulation [62] was used to account for the mesh motion, where the mesh velocity is a linear function with a value equal to the instantaneous piston velocity on the piston and decreasing to zero at the cylinder liner top. The first mesh was used from the intake valve closure at 130° bTDC (590 CAD) up to 40° bTDC (680 CAD) and the second grid from 680 CAD onwards. A scalable high-order spectral interpolation was employed in order to advance the solution from one grid to the next without compromising the high-order accuracy of the method. A high-order temporal integration splitting scheme for low-Mach number flows was used [63], where the hydrodynamic equations are advanced with a backward difference/characteristic-based time-stepping algorithm developed for the ALE method [64] allowing to overcome the Courant-Friedrichs-Lewy (CFL) restrictions imposed by standard schemes such as backward difference/extrapolation. Using this approach, variable time step sizes ranging from 0.2 to 0.5 μ s were achieved, or equivalently from 1100 to 450 time steps/CAD for the engine speed considered here. The total computational cost was close to 2.3 million CPU core-hours using up to 51,328 cores on the Argonne Leadership Computing Facility Knights Landing system *Theta*.

3.2 Comparison between LES and DNS

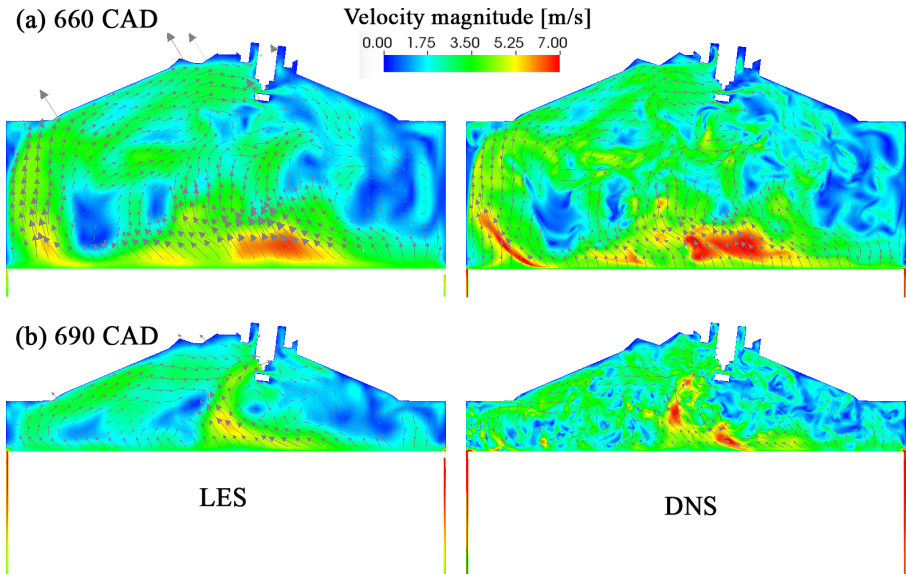


Fig. 6: Vectors and magnitude of instantaneous velocity on the tumble plane: comparison between SRS2 (left) and DNS (right) at (a) 60° bTDC and (b) 30° bTDC. The crevice is only partially depicted.

Figure 6 compares velocity vectors superimposed on the contour plots of the velocity magnitude on the tumble plane for the SRS2 (left) and the DNS (right) at two time instants during compression. The flow fields at 60° bTDC (Fig. 6(a)) correspond to a time approximately halfway through the compression stroke. At both time instants, a distinct clock-wise tumble motion can be discerned, which results from the strong intake flow and the pent-roof cylinder head geometry. As expected, the DNS exhibits additional small-scale structures, which are formed as the high wavenumber part of the energy spectrum (fully resolved in DNS but filtered in LES) is increasingly populated during compression. The consequence of the absence of small-scale turbulent structures is more pronounced later in the cycle as the simulation progresses towards TDC (Fig. 6(b)), where the Reynolds number is higher due to compression. In the SRS2 flow field the distinct tumble motion still persists, as opposed to the DNS where the tumble breakdown has already commenced. More details on the tumble vortex formation and the large-scale flow evolution in this engine can be found in [65].

3.3 Boundary layer evolution

3.3.1 Averaging procedure

The investigation of the flow evolution inside an ICE with DNS offers a unique opportunity for fundamental understanding of the relevant phenomena without relying on the individual models to account for sub-filter scale dissipation, wall shear stress and heat flux. On the downside, a single compression stroke was simulated due to the high computational costs of DNS. Hence, the results obtained suffer from the lack of comprehensive statistical significance, since only a single snapshot of the system state at each CAD can be provided, in contrast to the phase-averaging performed over many cycles in the experiments and SRS1. While the single-realization strategy adopted in the DNS is adequate for investigating in detail the flow topology and phenomenology, it is not sufficient to analyze the evolution of boundary layers during compression. To alleviate this difficulty, as an alternative to phase averaging over many cycles, a spatial averaging procedure was assessed with the help of the multi-cycle scale-resolving simulation (SRS1).

In most studies investigating boundary layers in canonical configurations, the adoption of spatial averaging techniques, in combination with time- and/or phase-averaging, is a common practice, since it allows for the reduction in the total simulation time needed to obtain converged statistics. A necessary first step in the process is the identification of a homogeneous direction, namely a direction where the flow exhibits similar properties, along which spatial averaging can be performed. Such directions are for example the azimuthal and stream-wise directions in the study of circular pipes [66], or the stream-wise and spanwise directions in channel flows [67]. In a complex flow such as that inside an ICE, such an averaging direction is not obvious. The cross-tumble

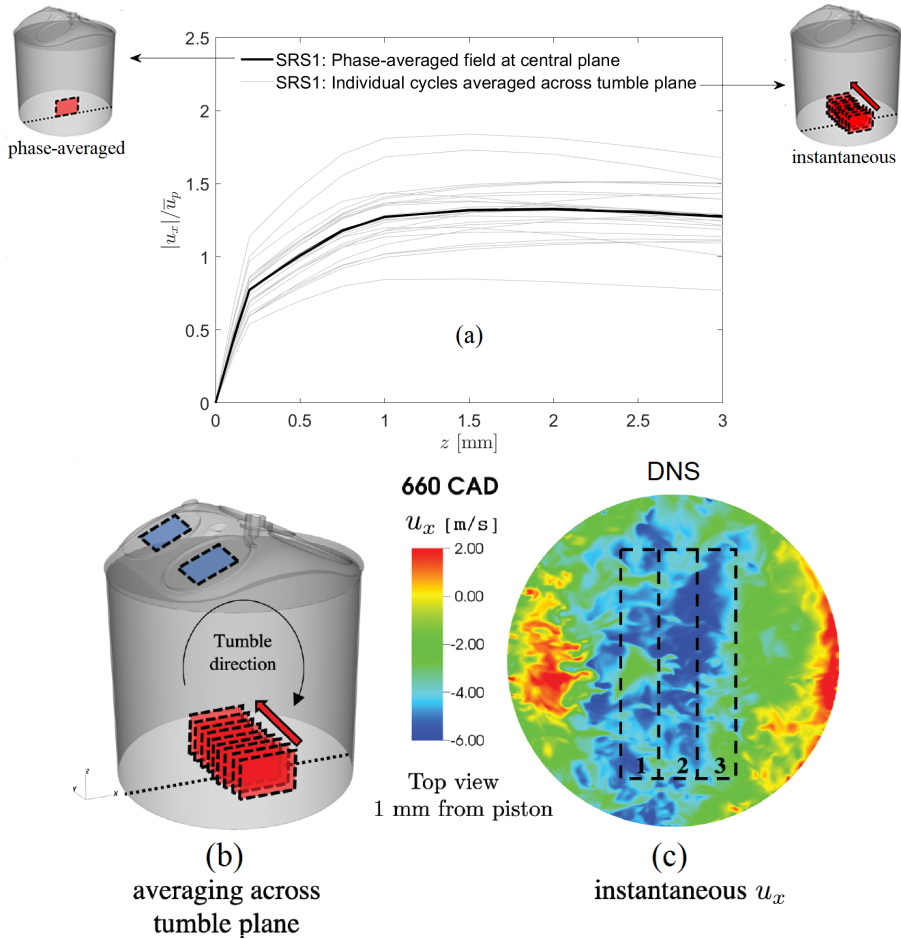


Fig. 7: Spatial averaging procedure employed for the extraction of boundary layer quantities from the DNS data: (a) near-piston stream-wise velocity profiles extracted from SRS1 using phase- (black lines) or spatial (gray lines) averaging, (b) schematic of the tumble direction with respect to the averaging planes employed in this work, and (c) instantaneous wall-parallel velocity component 1 mm away from the piston surface obtained from the DNS data. The blue rectangles in (b) and numbered black rectangles in (c) denote sampling domains referenced in the text.

(spanwise) direction was considered as a good candidate for the pent-roof cylinder head geometry considered here, and the rest of this section attempts to elucidate and justify this choice.

We start by examining the correspondence between a single cycle and the multi-cycle process. For SRS1, Fig. 7(a) displays the wall-normal profile of the piston-parallel velocity component formed through two processing

methods: (i) phase-averaging from the multi-cycle simulation at the central
 355 plane (similar to the processing of measurements), and (ii) spatial averaging
 of instantaneous fields from individual cycles. The results indicate that for the
 majority of the 25 cycles, the velocity profiles obtained by spatial averaging
 in the spanwise direction correspond well with the mid-plane, phase-averaged
 one. It should be acknowledged that there is substantial cycle-to-cycle variation
 360 in the large-scale tumble flow, inducing variation in both near-wall velocities
 and their spatial homogeneity. It is argued however that, while the DNS data
 cannot provide statistics fully equivalent to phase-averaging, the flow field is
 sufficiently representative of the multi-cycle process for further analysis and a
 meaningful comparison with experiments.

To further examine the sensitivity to the sampling domains, the spatial
 flow variation is considered from several perspectives. First, the sensitivity of
 the near-wall flow statistics to the post-processing domain size was examined.
 Figure 8 presents normalized and scaled wall-parallel velocity profiles as a
 function of the distance from the piston for different time instants during
 compression and for three sampling domains of different size centered at the
 cylinder axis. The inner scaling has been adopted for the transformation from
 physical to wall-normal units, where the scaled wall-normal coordinate is

$$z^+ = \frac{z}{\nu_w} u_\tau \quad (4)$$

and the scaled velocity

$$u^+ = \frac{u}{u_\tau} \quad (5)$$

with $u_\tau = \sqrt{\tau_w / \rho_w}$ the friction velocity, $\tau_w = \mu_w \partial u_x / \partial z$ the wall shear stress
 with μ_w , u_x the dynamic viscosity and stream-wise velocity component respec-
 tively, and ρ_w , ν_w the gas density and kinematic viscosity at the wall at the
 fixed coolant temperature of 333 K. The black dashed lines in Fig. 8(b) and
 in all subsequent figures represent the so-called law of the wall defined as [68]

$$u^+ = \begin{cases} z^+ & \text{if } z^+ < 10 \\ 1/\kappa \ln z^+ + B & \text{if } z^+ > 10 \end{cases} \quad (6)$$

365 where, $\kappa = 0.41$ is the von Karman constant and $B = 5.2$ the log-law constant.

The top, middle and bottom rows correspond to data sampling regions of
 increasing size. As can be observed, qualitatively similar trends are overall
 obtained for both the normalized and scaled velocities across different sampling
 domain sizes. The scaled profiles for the small sampling region in the upper
 370 right graph of Fig. 8 constitute an exception, indicating that the sample size
 for this region is small, such that localized flow patterns are pronounced in
 the collected statistics, as opposed to very similar profiles obtained for the two
 larger regions. Unless otherwise noted, the largest region (covering $3 \times 6 \text{ cm}^2$ of
 the piston surface area) was used to collect near-wall statistics on the piston
 375 surface.

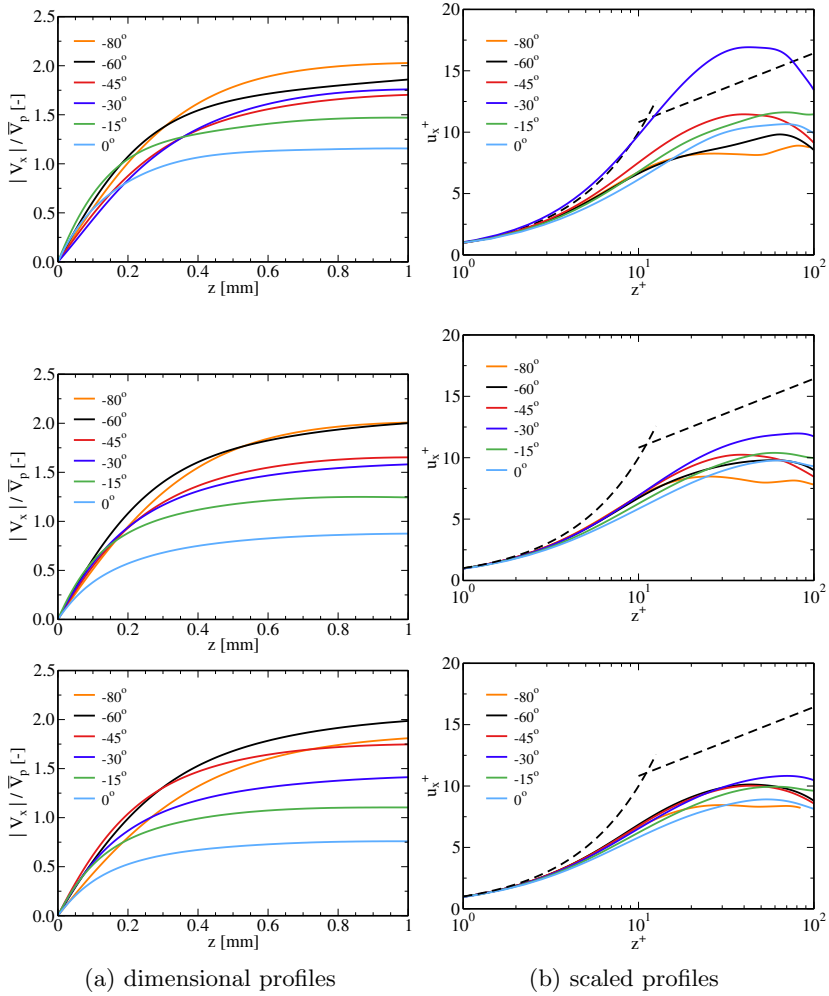


Fig. 8: (a) Normalized and (b) scaled wall-parallel velocity profiles as a function of the distance from the piston surface for sampling domain size of $1 \times 2 \text{ cm}^2$ (top), $2 \times 4 \text{ cm}^2$ (middle) and $3 \times 6 \text{ cm}^2$ (bottom).

3.3.2 Momentum boundary layer

Having established a post-processing workflow to extract near-wall statistics of the wall-parallel flow, we now compare the statistical behavior of the velocity profiles with those obtained from experiments. The evolution of the momentum boundary layer close to the piston surface as compression progresses is shown by the solid curves in Fig. 9 together with the corresponding profiles from the optical measurements (open symbols). Increasing velocity gradients are observed near the wall as a result of the decreasing kinematic viscosity and

the consequent increase in the Reynolds number, indicating that the boundary layer becomes thinner during compression (Fig. 9(a)). Furthermore, in contrast to canonical flow configurations no steady mean flow inside the cylinder exists and the velocity outside of the boundary layer (for example, at $z = 1$ mm) changes during compression, adapting to the continuously varying bulk flow due to the presence of the transient tumble motion within the cylinder. Overall, a good agreement is evident between the DNS and experimental data, especially considering the different approaches used to extract them (i.e. spatial vs. phase averaging).

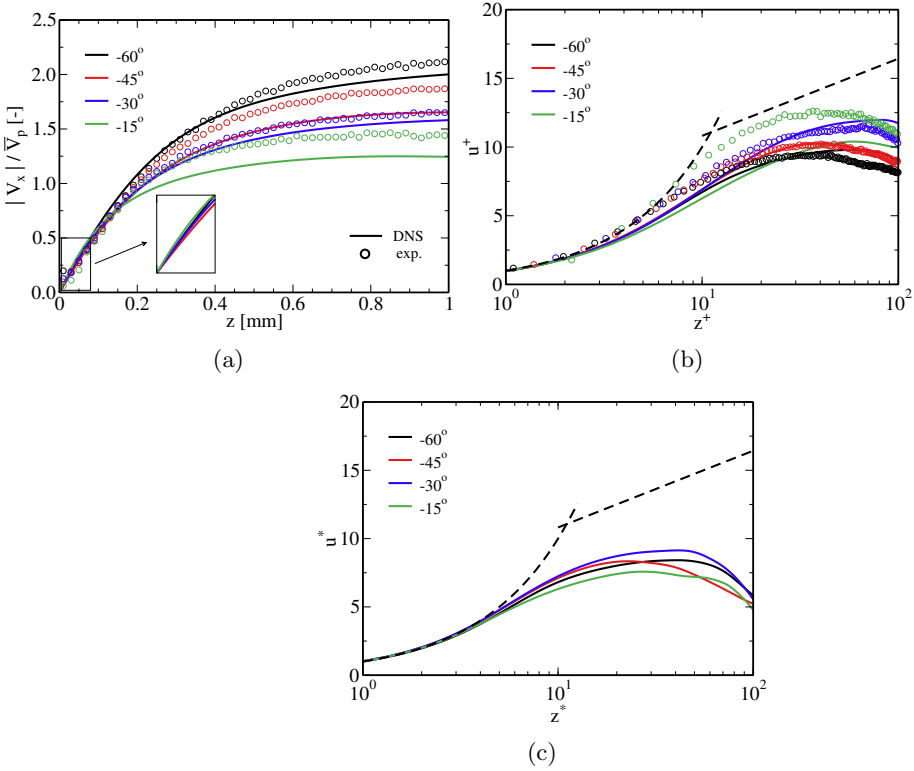


Fig. 9: Wall-parallel velocity profiles, normalized with the mean piston speed, as a function of the distance from the piston surface at different CAD during compression: (a) dimensional values, (b) inner-scaled values (Eqs. 4-5), (c) semi-local scaled values (Eqs. 7-8). The open symbols in all figures denote the experimental measurements [6] and solid lines represent the DNS results. The black dashed lines denote the profiles predicted by the law of the wall (Eqs. 6 and 9 for (b) and (c), respectively).

The scaled velocity profiles shown in Figs. 9(b) and (c) exhibit a rather universal behavior, especially when the density variation inside the boundary

layer is taken into account in the case of semi-local scaling

$$z^* = \frac{z}{\nu} \sqrt{\frac{\tau_w}{\rho}} \quad , \quad (7)$$

$$u^* = u \sqrt{\frac{\tau_w}{\rho}}^{-1} \quad (8)$$

with the corresponding law-of-the-wall

$$u^* = \begin{cases} z^* & \text{if } z^* < 10 \\ 1/\kappa \ln z^* + B & \text{if } z^* > 10 \end{cases} \quad (9)$$

where again, $\kappa = 0.41$ and $B = 5.2$. Indeed, curves corresponding to different time instants during compression collapse, albeit at values which differ significantly from those predicted by the law of the wall. They approximately follow the viscous sub-layer linear trend and start deviating thereafter, leading to values of up to 80% lower in the logarithmic region. In particular, the viscous sub-layer extent, commonly defined as the distance beyond which the scaled velocity profiles are not linear, depends heavily on whether the density variation across the boundary layer is taken into account. A comparison of the inner-scaled and semi-local scaled velocities in Figs. 9(b) and (c) respectively demonstrates a large increase of the linear region from $z^+ \approx 2$ to $z^* \approx 5$. This emphasizes the need for clear definition of the quantities and metrics used to characterize the boundary layer, especially when reporting results from non-isothermal flows.

The above-mentioned deviation from the law of the wall is in agreement with previous studies [8, 23, 38, 69] and confirm that algebraic wall-function models based on this scaling are not suitable for describing the evolution of ICE boundary layers, except perhaps in conditions they have been specifically tuned for. The deviation originates from the underlying assumptions introduced to derive these ideal laws, such as quasi-steady flow, high Reynolds number regime, and zero pressure gradient. To assess the importance of the latter, we split the observation region into three stream-wise sub-regions marked in Fig. 7(c).

A visualization of the velocity field on the tumble plane ($y = 0$ mm) and its spatial average is provided in Fig. 10 at different time instants during compression. The direction of the tumble-induced flow above the piston surface is from right to left, i.e. from region 3 to 1. The corresponding scaled velocity profiles are shown in Fig. 11 for the same time instants. Of interest here is the relation between those profiles and the flow stream-wise pressure gradient reported in the legend of each figure. We note that the known phenomenology from developing boundary layers is reflected, especially in the context of impinging flows (e.g. [70]). As the tumble vortex impinges on the piston surface, the flow experiences blockage close to the stagnation region that induces an adverse (positive) pressure gradient (APG) resulting in a “low” profile of u^+

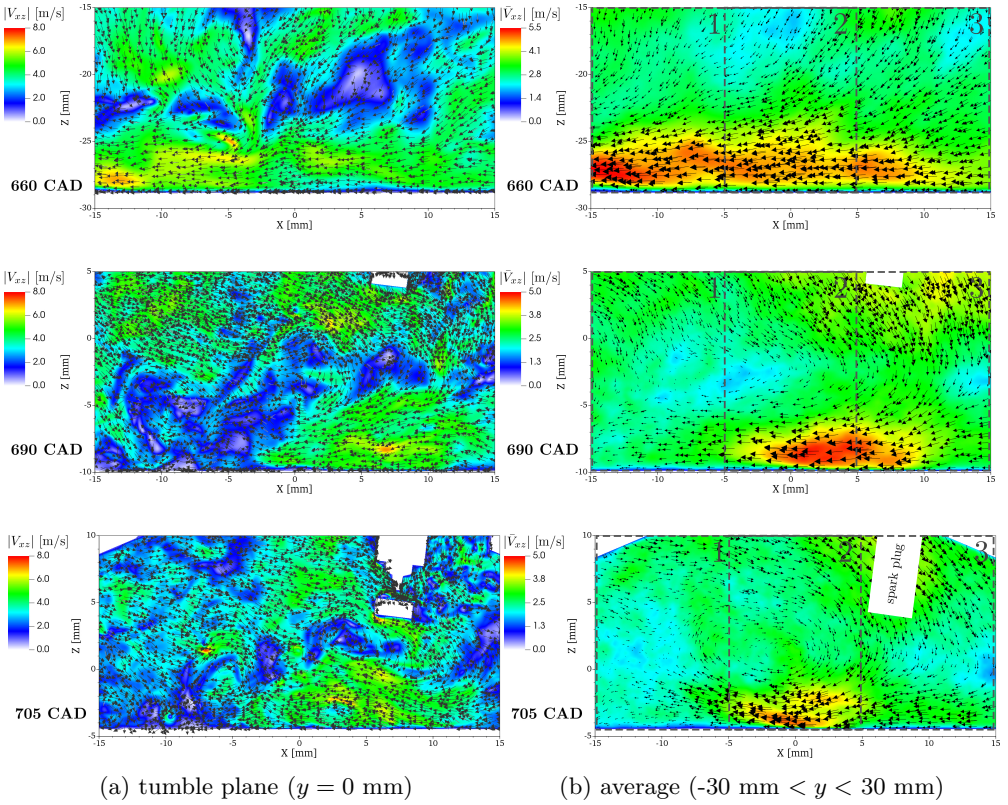


Fig. 10: In-plane velocity vectors and magnitude above the piston surface at different time instances (rows): (a) along the tumble plane ($y = 0$ mm) and (b) average across the tumble direction ($-30\text{mm} < y < 30\text{mm}$). The dashed gray lines in (b) denote the sub-regions 1 to 3, where the profiles of Fig. 11 were extracted.

(e.g. the green curve in all graphs of Fig. 11). Mean velocity profiles in developing turbulent boundary layers have been reported to lie below the log-law with increasing APG strength [71].

As the flow develops from region 2 to 1, a favorable (negative) pressure gradient is noted, which corresponds to profiles progressively approaching developed wall jets, leading to high values of u^+ . This brings further evidence towards the fact that the near-wall flow field not only deviates from ideal conditions, but does so also in a localized manner, suggesting that non-equilibrium factors such as the stream-wise pressure gradient have a strong effect. As a consequence, modeling the momentum boundary layer with a single wall function does not appear to be well-suited: the wall model should adopt non-equilibrium principles, or alternatively, the solution should be integrated to the wall, as in hybrid LES/RANS methods with a low-Reynolds turbulence model.

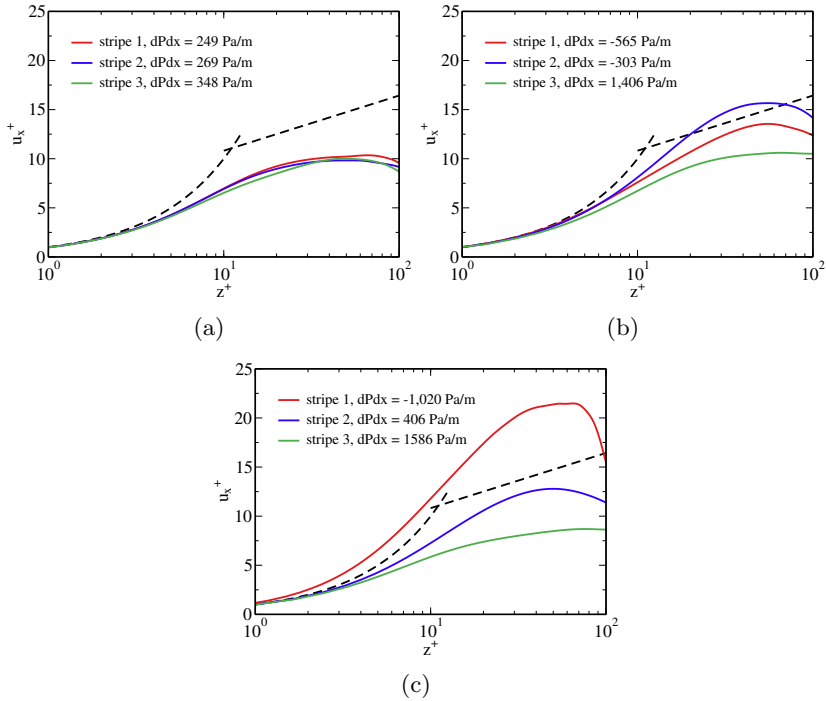


Fig. 11: Scaled wall-parallel velocity profiles as a function of the scaled distance from the piston surface for the sampling sub-regions shown in Figs. 7(c) and 10(b) at different time instances during compression: (a) 660 CAD, (b) 690 CAD and (c) 705 CAD. The corresponding values of the stream-wise pressure gradient are given in the legend.

In order to gain a better understanding of the near-wall turbulence characteristics and how they evolve and interact with the bulk flow during compression, the Favre-averaged Reynolds stress tensor components are shown in Fig. 12 at different CAD as compression progresses. By examining the diagonal stress components in Figs. 12(a), (c) and (e), a non-isotropic turbulent flow development in the wall vicinity is apparent. The stream-wise component $\overline{\rho u_x'' u_x''}$ exhibits an increasing trend with CAD, clearly affected by the deceleration-stagnation-acceleration mechanism discussed above. At the same time, the location of the peak values moves to higher z^+ distances towards the edge of the boundary layer. In contrast, rather constant profiles throughout the compression are encountered along the cross-tumble direction $\overline{\rho u_y'' u_y''}$. Only when the piston stops moving at 0 CAD a redistribution of turbulent kinetic energy seems to take place, and the two wall-parallel stress components acquire similar values towards two dimensional isotropy [72]. In the wall-normal direction, the piston motion induces a uniform flow directed upwards, suppressing the generation of turbulent fluctuations close to the wall, as evidenced by the

low stress values in Fig. 12(e). Consequently, the off-diagonal stress components involving vertical fluctuations u_z'' are also affected, leading to much lower values compared to the off-diagonal $\overline{\rho u_x'' u_y''}$ element that involves only wall-parallel stress components.

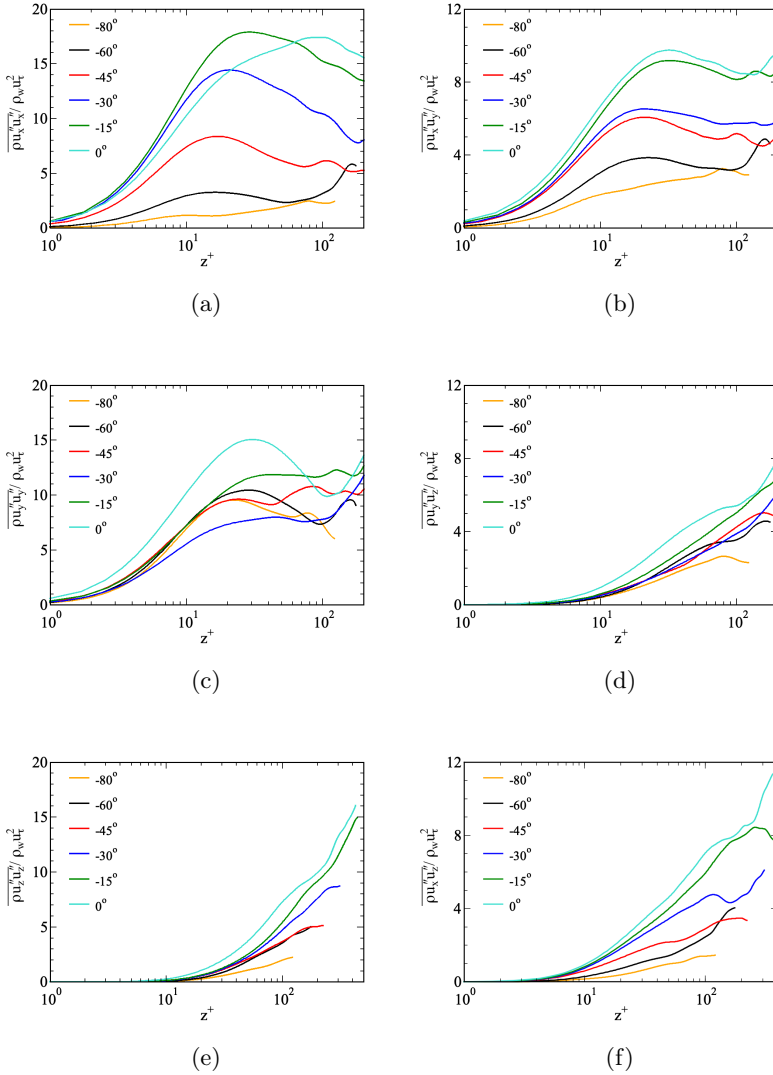


Fig. 12: Favre-averaged Reynolds stress tensor components at different CAD during compression for the $2 \times 4 \text{ cm}^2$ sampling domain: (a), (c), (e) diagonal components, (b), (d), (f) off-diagonal components.

In this tumble-dominated engine flow, the selected post-processing region features a clear, dominant flow direction that allowed to study the wall-parallel velocity statistics and compare with experimentally obtained values. However, in other regions and in engines without a tumble motion, it is often not meaningful to observe flow variables in a single direction. Instead, a magnitude-based processing is more appropriate, where the wall-parallel velocity magnitude $u_{xy} = \sqrt{u_x^2 + u_y^2}$ and wall shear stress $\tau_{wxy} = \mu_w \sqrt{\tau_{wx}^2 + \tau_{wy}^2}$ are used (the x - and y -direction denote the wall-parallel components). To monitor whether the boundary layer statistics change substantially between directional and magnitude-based processing, Fig. 13 presents the resulting dimensional and scaled velocity profiles close to the piston surface using both methods. As can be observed, they yield very similar profiles, and the magnitude-based processing can be used in the following to extract near-wall statistics from other regions of the engine.

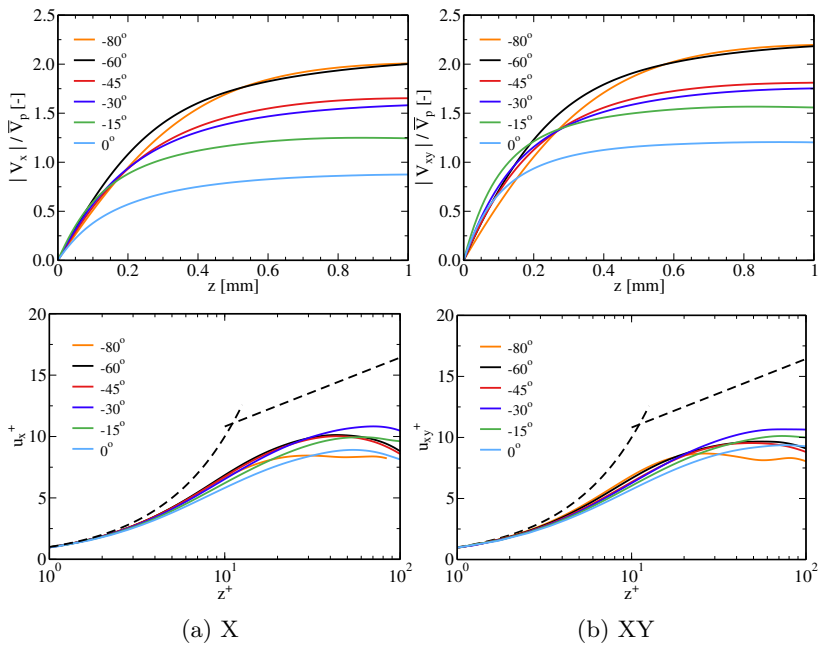


Fig. 13: Dimensional (top row) and scaled (bottom row) velocity profiles as a function of the distance from the piston surface using (a) directional and (b) magnitude-based processing.

The velocity profiles of Fig. 14 were extracted from a parallelepiped sampling region on the intake valve surfaces (blue regions in Fig. 7(left)). For brevity, results from one of the two intake valves are shown, but the trend is similar for all valves. The momentum boundary layer evolution is analogous

to the one observed along the piston surface, clearly indicating that near-wall flow deviations from ideal flow behavior are not restricted to the piston surface.

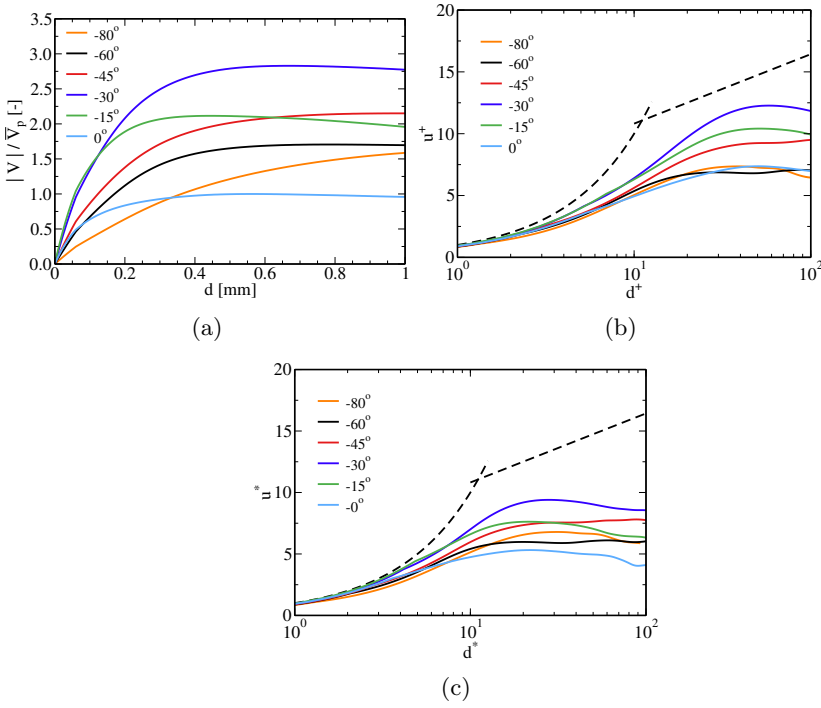


Fig. 14: Magnitude-based, wall-parallel velocity profiles as a function of the distance from the intake valve surface at different CAD during compression: (a) dimensional values, (b) inner-scaled values (Eqs. 4-5), (c) semi-local scaled values (Eqs. 7-8). The black dashed lines denote the profiles predicted by the law of the wall (Eqs. 6 and 9 for (b) and (c), respectively).

3.3.3 Thermal boundary layer

The evolution of temperature profiles as compression progresses is plotted as a function of the distance from the piston and valve surfaces in Figs. 15 and 16, respectively. The near-wall temperature gradients in the dimensional profiles of Figs. 15(a) and 16(a) increase monotonically during compression. Unlike the momentum boundary layers, the profiles flatten out with increasing distance from the wall to the increasing bulk values resulting from the pressure increase, and are unaffected by the rapidly varying bulk flow due to the tumble motion within the cylinder.

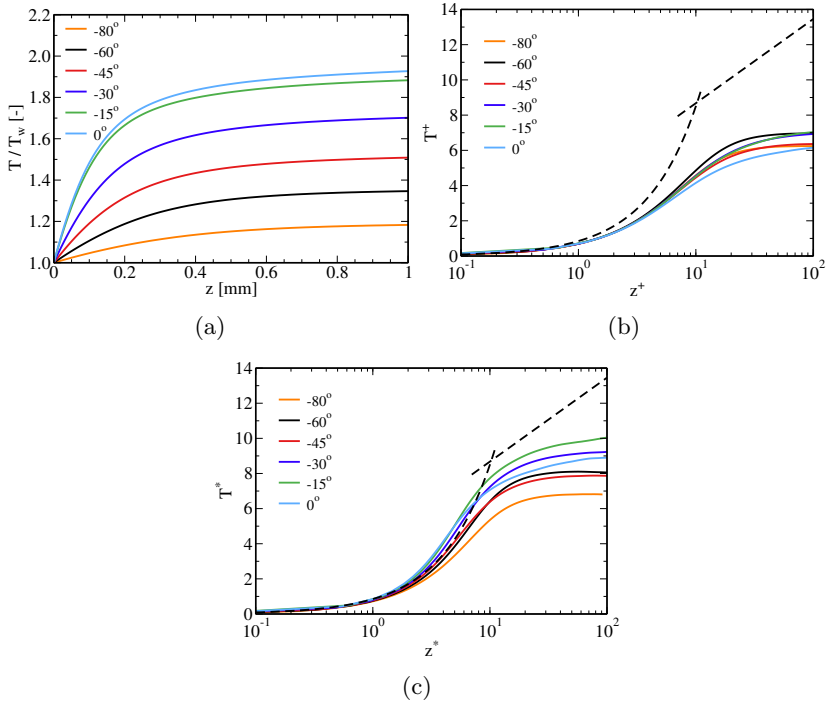


Fig. 15: Temperature as a function of the distance from the piston surface at different CAD during compression: (a) dimensional values, (b) inner-scaled values (Eqs. 4, 10), (c) semi-local scaled values (Eqs. 7, 11). The black dashed lines denote the profiles predicted by the thermal law of the wall (Eqs. 12 and 13 for (b) and (c), respectively).

Along with the inner and semi-local scaled temperature profiles

$$T^+ = \rho_w c_p (T_w - T) u_\tau / q_w \quad (10)$$

and

$$T^* = \rho_w c_p (T_w - T) \sqrt{\frac{\tau_w}{\rho}} / q_w \quad (11)$$

shown in Figs. ??, the thermal law of the wall [73]

$$T^+ = \begin{cases} z^+ \text{Pr} & \text{if } z^+ < 10 \\ 2.075 \ln z^+ + 3.9 & \text{if } z^+ > 10 \end{cases} \quad (12)$$

$$T^* = \begin{cases} z^* \text{Pr} & \text{if } z^* < 10 \\ 2.075 \ln z^* + 3.9 & \text{if } z^* > 10 \end{cases} \quad (13)$$

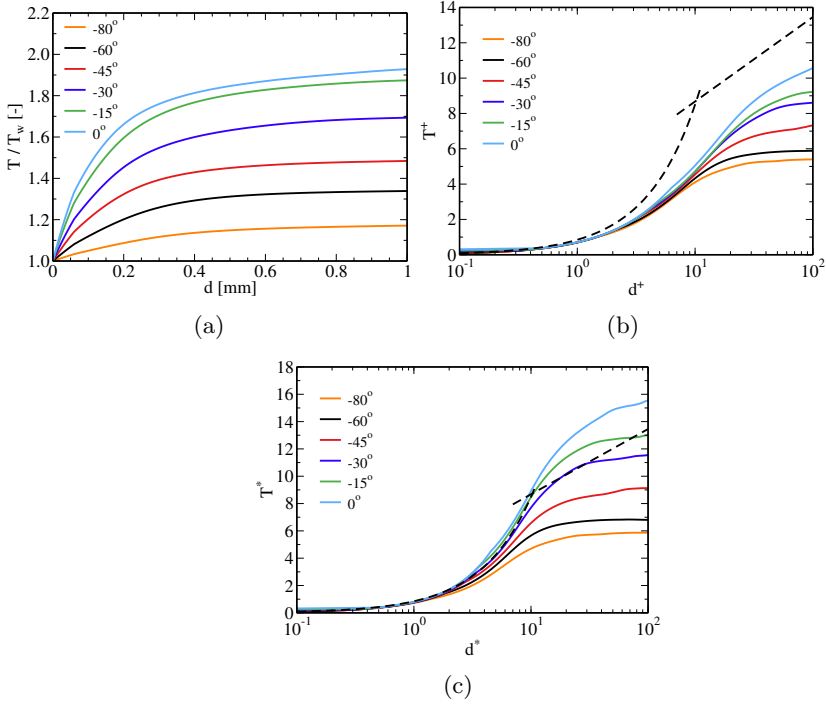


Fig. 16: Temperature as a function of the distance from the valve surface at different CAD during compression: (a) dimensional values, (b) inner-scaled values (Eqs. 4, 10), (c) semi-local scaled values (Eqs. 7, 11). The black dashed lines denote the profiles predicted by the thermal law of the wall (Eqs. 12 and 13 for (b) and (c), respectively).

is plotted in the same figures, where T_w is the temperature at the wall and $q_w = \lambda_w \partial T / \partial z$ the wall heat flux with λ_w the thermal conductivity at T_w . As can be observed, the thermal boundary layer also deviates considerably from the law of the wall for both investigated regions. A reasonable agreement is only noted in the viscous sublayer, especially when the density variation within the boundary layer is taken into account (Figs. 15(c), 16(c)). Notably, in contrast to observations in [38], where a consistent scaling between different time instances was achieved with the semi-local formulation, no such consistency is observed here. In fact, the curves span a wider range of values than the inner scaled ones. Since semi-local scalings for turbulent boundary layers have mainly been investigated in the context of fully developed flows (e.g. [36, 74, 75]), it is perhaps not surprising that the observed near-wall profiles do not collapse with such scaling.

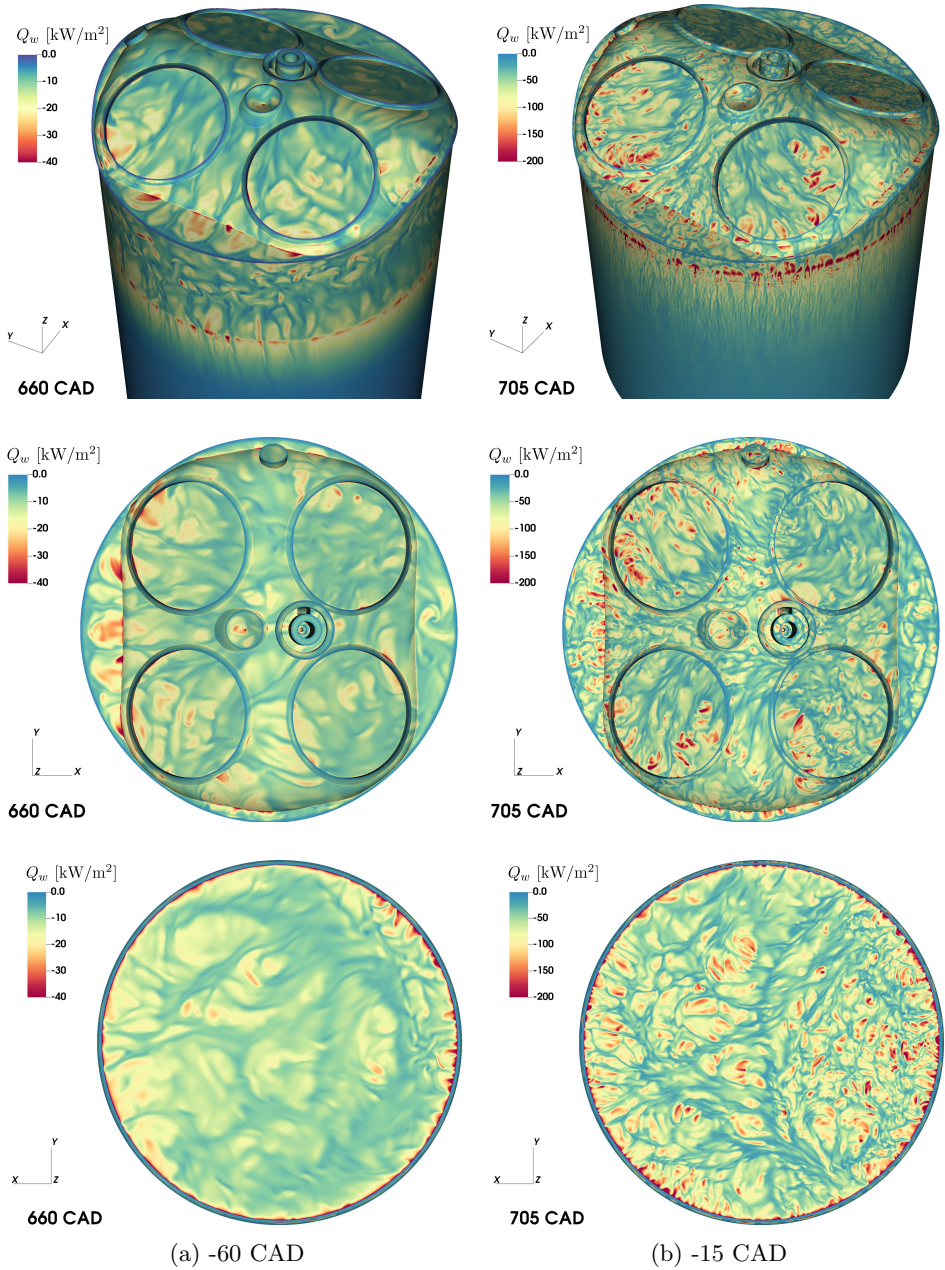


Fig. 17: Iso-contours of heat flux along the cylinder walls at (a) -60° bTDC and (b) -15° bTDC. Top: bird's eye view, middle: cylinder head view, bottom: piston view.

3.3.4 Wall heat flux

To provide a qualitative understanding of the heat flux behavior and its distribution across different regions of the engine, Fig. 17 presents isocontours of the wall heat flux on the cylinder liner, head and piston surfaces at two time instants: half-way through (660 CAD, left column) and towards the end (705 CAD, right column) of compression. In general, the correlation between the flow and heat flux scales is evident, where finer heat flux structures are observed as the Reynolds number increases due to compression. In agreement with [42], higher heat fluxes are noted at regions where the flow is predominantly impinging/stagnating, as for example evidenced by the higher values at the right part of the piston surface compared to the left (bottom right graph in Fig. 17), which is the impingement region of the tumble vortex into the piston. For the same reason, the heat flux is higher on the left part of the cylinder head.

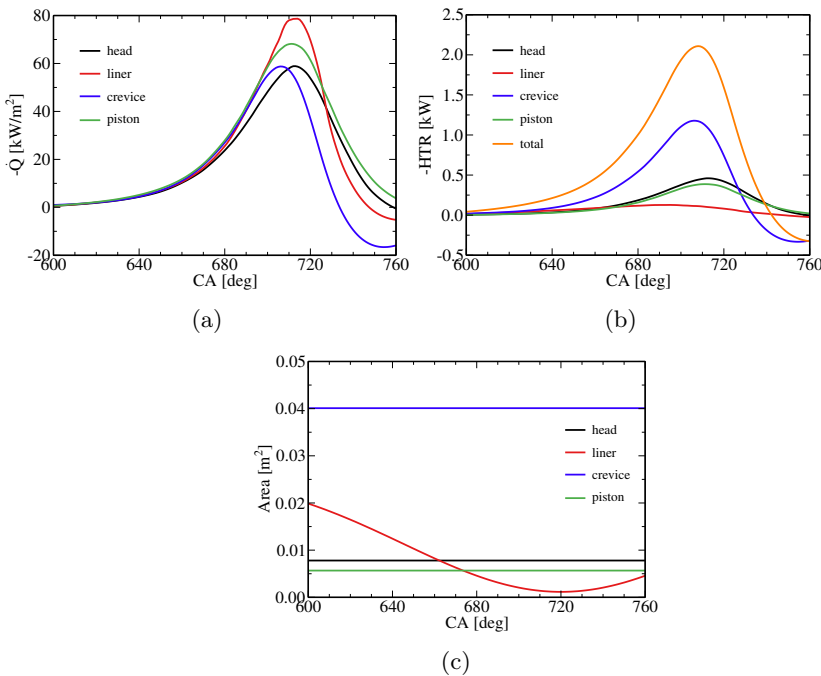


Fig. 18: Evolution of the component-wise (a) heat flux, (b) heat transfer rate and (b) area during compression.

Furthermore, significant heat flux values are noted at the entrance of the piston-liner crevice volume (top row in Fig.17) as a result of the intense, jet flow in this region. In fact, the crevice volume is the largest contributor in the total heat losses, as shown by the evolution of the transfer rate on different

surfaces in Fig. 18(b). It is important to note however, that the enlarged piston clearance and the lower positioning of the piston rings in this optical setup are not representative of production engines. Nevertheless, the study of crevice flows in general is an interesting topic, regarding not only heat transfer aspects but also pollutant emissions [76].

Finally, in terms of the global metrics shown in Fig. 18(a), heat fluxes on different parts of the domain are on the same order of magnitude. However, due its much larger surface area (at least twice than the liner and more than four times the piston/head), the crevice dominates the process.

4 Conclusions

In this study, a workflow that exploits the complementarity between state-of-the-art optical diagnostics, scale-resolving and fully resolved direct numerical simulations was developed to investigate the flow evolution in internal combustion engines, with focus on the near-wall phenomena. Through validation of multi-cycle scale-resolving simulations against experimental measurements, realistic and well-characterized initial conditions were generated that enabled the DNS of a single compression stroke. After carefully assessing the methodology, representative statistics were extracted from the DNS data to analyze the evolution of the momentum and thermal boundary layers at different engine regions.

The flow statistics were found to deviate considerably from ideal scenarios, such as those described by the law of the wall. Phenomenologically, they are similar to those for developing boundary layers, particularly for impinging flows. As the intake-induced large scale directed flow (i.e. tumble vortex) approaches the cylinder walls, it experiences a deceleration–stagnation–acceleration process, leading to a dynamically changing boundary layer (BL) behavior, not only temporally but also locally. Consequently, these fluctuations give rise to alternating stream-wise pressure gradients, eventually rendering invalid the flow equilibrium assumptions commonly adopted in many wall-modeling approaches. This suggests that for the investigation of ICE flows and in similar configurations, a wall model should adopt non-equilibrium principles. An analysis of the Reynolds stress components during compression revealed a complex, anisotropic turbulence generation mechanism in the wall vicinity, affected both by the presence of the tumble motion and the uniform upward flow induced by the piston motion.

The high resolution DNS also allowed the investigation of the thermal boundary layers and their evolution, which were also found to deviate considerably from ideal scaling laws, even with the use of scaling that accounts for variation of the fluid material properties within the boundary layer. Inspection of the heat flux distribution confirmed the similarity between the flow and heat flux patterns and identified regions of intense heat flux, mainly in places of strong directed flow against the wall. Such a region is the entrance to the crevice, which, in the optical engine configuration and for the motored

conditions considered in this study, accounts for most of the heat lost through convective transfer.

A possible reason for many of the above observations is the relatively low Reynolds number in the chosen (low) engine speed and throttled conditions. Wall-resolved simulation campaigns at higher engine speed and intake pressure adopting the methodology proposed here are currently underway. Furthermore, the generated data was used together with DNS results from different setups to develop an algebraic [77] and a data-driven neural network [78] model for wall heat transfer. Comparisons with the present dataset will prove useful in further identifying dependencies, derive scaling laws, as well as enable a priori and a posteriori model testing.

Even within its limitations, this work constitutes a first step towards the next generation of internal combustion engine simulations and paves the way for detailed investigations of more complex phenomena in the future, such as fired engine operation. In tandem, the computational cost limitations are being addressed through continuous evolution of the solver capabilities, with the aim to prepare for the next generation of hardware architectures, allowing the direct numerical simulation of more demanding conditions.

Acknowledgements This research used resources of the Argonne Leadership Computing Facility, which is a DOE Office of Science User Facility supported under Contract DE-AC02-06CH11357. Preliminary simulations were performed at the Swiss National Supercomputing Center (CSCS) under project ID 753. Financial support from the Forschungsvereinigung Verbrennungskraftmaschinen (FVV, project no. 1286: “Wall heat transfer processes in spark ignition engines”), the Swiss Federal Office of Energy (BfE, contract no. SI/501615-01), and the Swiss Competence Center for Energy Research - Efficient Technologies and Systems for Mobility (SCCER Mobility) is gratefully acknowledged. C.E.F. acknowledges the European Union’s Horizon 2020 research and innovation program under the Center of Excellence in Combustion (CoEC) project, grant agreement no. 952181.

Compliance with Ethical Standards

The authors declare that they have no conflict of interest.

References

- [1] Heywood, J.B.: Internal Combustion Engine Fundamentals. McGraw-Hill, New York (1988)
- [2] Lumley, J.L.: Engines: An Introduction. Cambridge University Press, Cambridge (1999)
- [3] Borée, J., Miles, P.C.: In-cylinder Flow. In: Encyclopedia of Automotive Engineering, John Wiley & Sons, Ltd, ??? (2014)

- [4] Arcoumanis, C., Whitelaw, J.H.: Fluid mechanics of internal combustion engines. *Proc. Inst. Mech. Eng.* **201** (1987)
- [5] Borman, G., Nishiwaki, K.: Internal Combustion Engine Heat Transfer. *Prog. Energy Combust. Sci.* **13**(1), 1–46 (1987)
- 605 [6] Renaud, A., Ding, C.-P., Jakirlic, S., Dreizler, A., Böhm, B.: Experimental characterization of the velocity boundary layer in a motored IC engine. *Int. J. Heat Fluid Flow* **71**, 366–377 (2018)
- [7] Alharbi, A.Y., Sick, V.: Investigation of boundary layers in internal combustion engines using a hybrid algorithm of high speed micro-PIV and PTV. *Exp. Fluids* **49**, 949–959 (2010)
- 610 [8] Jainski, C., Lu, L., Dreizler, A., Sick, V.: High-speed micro particle image velocimetry studies of boundary-layer flows in a direct-injection engine. *Int. J. Engine Res.* **14**(3), 247–259 (2013)
- [9] Peterson, B., Baum, E., Böhm, B., Sick, V., Dreizler, A.: High-speed PIV and LIF imaging of temperature stratification in an internal combustion engine. *Proc. Combust. Inst.* **34**(2), 3653–3660 (2013)
- 615 [10] Haworth, D.C.: Large-eddy simulation of in-cylinder flows. *Oil Gas Sci. Technol.* **54**(2) (1999)
- [11] Schiffmann, P., Gupta, S., Reuss, D., Sick, V., Yang, X., Kuo, T.W.: TCC-III engine benchmark for Large-Eddy Simulation of IC engine flows. *Oil Gas Sci. Technol.* **71**(1) (2016)
- 620 [12] Baum, E., Peterson, B., Böhm, B., Dreizler, A.: On The Validation of LES Applied to Internal Combustion Engine Flows: Part 1: Comprehensive Experimental Database. *Flow Turbul. Combust.* **92**(2), 269–297 (2014)
- 625 [13] Baumann, M., Mare, F.D., Janicka, J.: On the Validation of Large Eddy Simulation Applied to Internal Combustion Engine Flows Part II: Numerical Analysis. *Flow Turbul. Combust.* **92**(1), 299–317 (2014)
- [14] Mare, F.D., Knappstein, R., Baumann, M.: Application of LES-quality criteria to internal combustion engine flows. *Comput. Fluids* **89**, 200–213 (2014)
- 630 [15] Nguyen, T., Janas, P., Lucchini, T., D’Errico, G., Kaiser, S., Kempf, A.: LES of Flow Processes in an SI Engine Using Two Approaches: OpenFoam and PsiPhi. *SAE Technical Paper 2014-01-1121* (2014)
- [16] Janas, P., Wlokas, I., Böhm, B., Kempf, A.: On the evolution of the flow field in a spark ignition engine. *Flow Turbul. Combust.* **98**(1), 237–264
- 635

(2017)

- [17] He, C., Leudesdorff, W., Mare, F.D., Sadiki, A., Janicka, J.: Analysis of In-cylinder Flow Field Anisotropy in IC Engine using Large Eddy Simulation. *Flow Turbul. Combust.* **99**(2), 353–383 (2017)
- 640 [18] Buhl, S., Hain, D., Hartmann, F., Hasse, C.: A comparative study of intake and exhaust port modeling strategies for scale-resolving engine simulations. *Int. J. Engine Res.* **19**(3), 282–292 (2017)
- [19] Janas, P., Ribeiro, M.D., Kempf, A., Schild, M., Kaiser, S.: Penetration of the Flame Into the Top-Land Crevice - Large-Eddy Simulation and
645 Experimental High-Speed Visualization. SAE Technical Paper 2015-01-1907 (2015)
- [20] Bose, S.T., Park, G.I.: Wall-modeled large-eddy simulation for complex turbulent flows. *Ann. Rev. Fluid Mech.* **50**, 535–561 (2018)
- [21] Larsson, J., Kawai, S., Bodart, J., Bermejo-Moreno, I.: Large eddy simulation with modeled wall-stress: recent progress and future directions.
650 *Mech. Eng. Rev.* **3**(1), 15–00418 (2016)
- [22] Yang, X.I., Park, G.I., Moin, P.: Log-layer mismatch and modeling of the fluctuating wall stress in wall-modeled large-eddy simulations. *Phys. Rev. Fluids* **2**(10), 104601 (2017)
- 655 [23] Lav, C., Sandberg, R.D., Tanimoto, K., Terakado, K.: Pulsed impinging jets: Momentum and heat-transfer. *Int. J. Heat Mass Transfer* **187**, 122548 (2022)
- [24] Hohenberg, G.F.: Advanced approaches for heat transfer calculations. SAE Transactions, 2788–2806 (1979)
- 660 [25] Woschni, G.: A universally applicable equation for the instantaneous heat transfer coefficient in the internal combustion engine. SAE Technical paper 670931 (1967)
- [26] Chiodi, M., Bargende, M.: Improvement of engine heat-transfer calculation in the three-dimensional simulation using a phenomenological
665 heat-transfer model. SAE Technical Paper 2001-01-3601 (2001)
- [27] Han, Z., Reitz, R.D.: A temperature wall function formulation for variable-density turbulent flows with application to engine convective heat transfer modeling. *Int. J. Heat Mass Transfer* **40**(3), 613–625 (1997)
- [28] Angelberger, C., Poinso, T., Delhay, B.: Improving Near-Wall Combustion and Wall Heat Transfer Modeling in SI Engine Computations. SAE
670

Technical Paper 972881 (1997)

- [29] Werner, H., Wengle, H.: Large-eddy simulation of turbulent flow over and around a cube in a plate channel. In: *Turbulent Shear Flows 8*, pp. 155–168. Springer, ??? (1993)

- 675 [30] Plengsaard, C., Rutland, C.: Improved Engine Wall Models for Large Eddy Simulation (LES). SAE Technical Paper 2013-01-1097 (2013)

- [31] Keskinen, K., Nuutinen, M., Kaario, O., Vuorinen, V., Koch, J., Wright, Y.M., Larmi, M., Boulouchos, K.: Hybrid LES/RANS with wall treatment in tangential and impinging flow configurations. *Int. J. Heat Fluid Flow* **65**, 141–158 (2017)

- 680 [32] Park, G.I.: Wall-modeled large-eddy simulation of a high Reynolds number separating and reattaching flow. *AIAA Journal*, 3709–3721 (2017)

- [33] Yang, X.I., Sadique, J., Mittal, R., Meneveau, C.: Integral wall model for large eddy simulations of wall-bounded turbulent flows. *Phys. Fluids* **27**(2), 025112 (2015)

- 685 [34] Catchirayer, M., Boussuge, J.-F., Sagaut, P., Montagnac, M., Papadogiannis, D., Garnaud, X.: Extended integral wall-model for large-eddy simulations of compressible wall-bounded turbulent flows. *Phys. Fluids* **30**(6), 065106 (2018)

- 690 [35] Bae, H.J., Lozano-Durán, A., Bose, S.T., Moin, P.: Dynamic slip wall model for large-eddy simulation. *J. Fluid Mech.* **859**, 400–432 (2019)

- [36] Trettel, A., Larsson, J.: Mean velocity scaling for compressible wall turbulence with heat transfer. *Phys. Fluids* **28**(2), 026102 (2016)

- 695 [37] Yang, X.I., Lv, Y.: A semi-locally scaled eddy viscosity formulation for les wall models and flows at high speeds. *Theor. Comput. Fluid Dyn.* **32**(5), 617–627 (2018)

- [38] Schmitt, M., Frouzakis, C.E., Tomboulides, A.G., Wright, Y.M., Boulouchos, K.: Direct numerical simulation of the compression stroke under engine-relevant conditions: Evolution of the velocity and thermal boundary layers. *Int. J. Heat Mass Transfer* **91**, 948–960 (2015)

- 700 [39] Frouzakis, C.E., Giannakopoulos, G.K., Wright, Y.M., Boulouchos, K., Schmitt, M., Tomboulides, A.G.: Direct Numerical Simulations for Internal Combustion Premixed Gas Engines: First Steps, Challenges and Prospects. In: Leipert, A. (ed.) *Engine Combustion Processes - Current Problems and Modern Techniques*, pp. 267–284. Erlangen: ESYTEC-Verlag, ??? (2017)

- [40] Schmitt, M., Frouzakis, C.E., Wright, Y.M., Tomboulides, A.G., Boulouchos, K.: Investigation of wall heat transfer and thermal stratification under engine-relevant conditions using DNS. *Int. J. Engine Res.* **17**, 63–75 (2015)
- [41] Schmitt, M., Frouzakis, C.E., Tomboulides, A.G., Wright, Y.M., Boulouchos, K.: Direct numerical simulation of the effect of compression on the flow, temperature and composition under engine-like conditions. *Proc. Combust. Inst.* **35**(3), 3069–3077 (2015)
- [42] Schmitt, M., Frouzakis, C.E., Wright, Y.M., Tomboulides, A.G., Boulouchos, K.: Direct numerical simulation of the compression stroke under engine relevant conditions: Local wall heat flux distribution. *Int. J. Heat Mass Transfer* **91**, 948–960 (2015)
- [43] Schmitt, M., Boulouchos, K.: Role of the intake generated thermal stratification on the temperature distribution at top dead center of the compression stroke. *Int. J. Engine Res.* **17**(8), 836–845 (2016)
- [44] Ma, P.C., Greene, M., Sick, V., Ihme, M.: Non-equilibrium wall-modeling for internal combustion engine simulations with wall heat transfer. *Int. J. Eng. Res.* **18**(1-2), 15–25 (2017)
- [45] Keskinen, K., Koch, J., Wright, Y.M., Schmitt, M., Nuutinen, M., Kaario, O., Vuorinen, V., Larmi, M., Boulouchos, K.: Numerical assessment of wall modelling approaches in scale-resolving in-cylinder simulations. *Int. J. Heat Fluid Flow* **74**, 154–172 (2018)
- [46] Giannakopoulos, G.K., Frouzakis, C.E., Fischer, P.F., Tomboulides, A.G., Boulouchos, K.: LES of the gas–exchange process inside an internal combustion engine using a high-order method. *Flow Turbul. Combust.* **104**, 673–692 (2020)
- [47] Baumann, M., Di Mare, F., Janicka, J.: On the validation of large eddy simulation applied to internal combustion engine flows part II: numerical analysis. *Flow Turbul. Combust.* **92**(1-2), 299–317 (2014)
- [48] Nguyen, T.M., Proch, F., Wlokas, I., Kempf, A.M.: Large eddy simulation of an internal combustion engine using an efficient immersed boundary technique . *Flow Turbul. Combust.* **97** (2016)
- [49] Rutland, C.J.: Large-eddy simulations for internal combustion engines - a review. *Int. J. Engine Res.* **12**(421) (2011)
- [50] Welch, C., Schmidt, M., Keskinen, K., Giannakopoulos, G., Boulouchos, K., Dreizler, A., Böhm, B.: The effects of intake pressure on in-cylinder gas velocities in an optically accessible single-cylinder research engine.

SAE Technical Paper, No. 2020-01-0792 (2020)

- 745 [51] Hasse, C., Sohm, V., Durst, B.: Numerical investigation of cyclic variations in gasoline engines using a hybrid URANS/LES modeling approach. *Comput. Fluids* **39**(1), 25–48 (2010)
- [52] Spalding, D.B.: A single formula for the “law of the wall”. *J. Appl. Mech.* **28**(3), 455–458 (1961)
- 750 [53] Plengsaard, C., Rutland, C.: Improved engine wall models for large eddy simulation (LES). SAE Technical Paper 2013-01-1097 (2013)
- [54] Liu, K., Haworth, D.C.: Development and assessment of POD for analysis of turbulent flow in piston engines. SAE Technical Paper 2011-01-0830 (2011)
- 755 [55] Shekhawat, Y., Paltrinieri, S., Schiffmann, P., Haworth, D., Fontanesi, S., Reuss, D., Sick, V.: An experimental and simulation study of turbulent flow in a homogeneous-charge spark-ignition engine. In: *LES for Internal Combustion Engine Flows (LES4ICE)* - Rueil-Malmaison (2014)
- [56] Buhl, S., Gleiss, F., Köhler, M., Hartmann, F., Messig, D., Brücker, C.,
760 Hasse, C.: A combined numerical and experimental study of the 3D tumble structure and piston boundary layer development during the intake stroke of a gasoline engine. *Flow Turbul. Combust.* **98**(2), 579–600 (2017)
- [57] Deville, M.O., Fischer, P.F., Mund, E.H.: *High-Order Methods for Incompressible Fluid Flow*. High-Order Methods for Incompressible Fluid Flow, Cambridge (2002)
- 765 [58] NEK5000 Version v17.0. Argonne National Laboratory, IL, U.S.A. Available at <https://nek5000.mcs.anl.gov>
- [59] Schmitt, M., Frouzakis, C.E., Tomboulides, A.G., Wright, Y.M., Boulouchos, K.: Direct numerical simulation of multiple cycles in a valve/piston
770 assembly. *Phys. Fluids* **26**(3) (2014)
- [60] Giannakopoulos, G.K., Frouzakis, C.E., Boulouchos, K., Fischer, P.F., Tomboulides, A.G.: Direct numerical simulation of the flow in the intake pipe of an internal combustion engine. *Int. J. Heat Fluid Flow* **68**(421) (2017)
- 775 [61] Trelis CFD v16.3. Csimsoft. <https://www.csimsoft.com/trelis-cfd>
- [62] Ho, L.W., Patera, A.T.: A Legendre spectral element method for simulation of unsteady incompressible viscous free-surface flows. *Comput. Meth. Appl. Mech. Eng.* **80**(1–3), 355–366 (1990)

- [63] Tomboulides, A.G., Lee, J., Orszag, S.: Numerical simulation of low Mach number reactive flows. *J. Sci. Comput.* **12**(139) (1997)
- [64] Patel, S., Fischer, P.F., Min, M., Tomboulides, A.G.: A characteristic-based spectral element method for moving-domain problems. *J. Sci. Comput.* (2018)
- [65] Müller, S.H.R., Böhm, B., M.Gleißner, R., Grzeszik, R., Arndt, S., Dreizler, A.: Flow field measurements in an optically accessible, direct-injection spray-guided internal combustion engine using high-speed PIV. *Experiments in Fluids* **48**, 281–290 (2010)
- [66] Noorani, A., Khoury, G.K.E., Schlatter, P.: Evolution of turbulence characteristics from stright to curved pipes. *Int. J. Heat Fluid Flow* **41**, 16–26 (2013)
- [67] Kim, J., Moin, P., Moser, R.: Turbulence statistics in fully developed channel flow at low Reynolds number. *J. Fluid Mech.* **177**, 133–166 (1987)
- [68] Pope, S.B.: *Turbulent Flows*. Cambridge University Press, ??? (2000)
- [69] Ma, P.C., Ewan, T., Jainski, C., Lu, L., Dreizler, A., Sick, V., Ihme, M.: Development and analysis of wall models for internal combustion engine simulations using high-speed micro-PIV measurements. *Flow Turbul. Combust.* **98**(1) (2016)
- [70] Hattori, H., Nagano, Y.: Direct numerical simulation of turbulent heat transfer in plane impinging jet. *Int. J. Heat Fluid Flow* **25**(5), 749–758 (2004)
- [71] Monty, J.P., Harun, Z., Marusic, I.: A parametric study of adverse pressure gradient turbulent boundary layers. *Int. J. Heat Fluid Flow* **32**(3), 575–585 (2011)
- [72] Choi, K.-S., Lumley, J.L.: The return to isotropy of homogeneous turbulence. *J. fluid Mech.* **436**, 59–84 (2001)
- [73] Bradshaw, P., Huang, G.P.: The law of the wall in turbulent flow. *Proc. R. Soc. Lond. A* **451**, 165–188 (1995)
- [74] Huang, P.C., Coleman, G.N., Bradshaw, P.: Compressible turbulent channel flows: DNS results and modelling. *J. Fluid Mech.* **305**, 185–218 (1995)
- [75] Patel, A., Peeters, J.W.R., Boersma, B.J., Pecnik, R.: Semi-local scaling and turbulence modulation in variable property turbulent channel flows. *Phys. Fluids* **27**(9), 095101 (2015)

- [76] Min, K., Cheng, W.K., Heywood, J.B.: The Effects of Crevices on the Engine-Out Hydrocarbon Emissions in SI Engines. SAE Transactions **103**(3), 371–385 (1994)
- [77] Bolla, M., Impagnatiello, M., Keskinen, K., Giannakopoulos, G.K., Frouzakis, C.E., Wright, Y.M., Boulouchos, K.: Development of an algebraic wall heat transfer model for LES in IC engines using DNS data. Proc. Combust. Inst. **38**, 5811–5819 (2021)
- [78] Impagnatiello, M., Bolla, M., Keskinen, K., Giannakopoulos, G., Frouzakis, C.E., Wright, Y.M., Boulouchos, K.: Systematic assessment of data-driven approaches for wall heat transfer modelling for LES in IC engines using DNS data. Int. J. Heat Mass Transfer **183**, 122109 (2022)